Structural and Multidisciplinary Optimization (2025) 68:31
https://doi.org/10.1007/s00158-024-03944-2

RESEARCH PAPER

Topology optimization for pressurized nonlinear structures using substructure and experimental studies

Yifu Lu[1] · Quantian Luo[1] · Liyong Tong[1]

Received: 20 June 2024 / Revised: 14 November 2024 / Accepted: 25 November 2024 / Published online: 15 February 2025

Abstract
A compliant structure under fluidic pressure can undergo relatively large shape change, but the design of such type of structure is challenging as the pressure distribution depends on detailed structural geometry. In this study, a novel mixed substructure-density (MSD) model is proposed for topology representation and update in the optimal design of nonlinear compliant structures under quasi-static fluidic pressure. An optimization algorithm is developed via implementing the present model by using super-elements in commercial finite element analysis (FEA) software. Numerical examples are presented to validate the present model, algorithm, and designs numerically via full linear and nonlinear FEAs. A planar cellular network with five cells arranged in parallel is then designed for representing a pressurized wing rib structure capable of modulating airfoil thickness variation. The test results of the single-cell and five-cell PCS specimens prototyped using polyurethane material show that the respective cell thickness can be reduced by 11.9 and 6.4% respectively under a cell pressure of 250 kPa.

Keywords Topology optimization · Substructure · Nonlinear analysis · Compliant mechanism · Design-dependent load

1 Introduction

Understanding and mimicking the biomimetic principles for designing and manufacturing innovative structure systems remains a significant challenge (Knippers and Speck 2012; Lienhard et al. 2011; Schleicher et al. 2015). Internal pressure regulation is one of such biomimetic principles observed in nature for structural adaptation. Pressure-actuated adaptation has been inspirational in the quest of searching for compliant structure systems capable of achieving large and smooth shape variations. Such a compliant structure system generally has less part count, can be fabricated using additive manufacturing, and operates cost-effectively, as compared to a traditional mechanism with hinged links. To optimize compliant mechanisms subjected to pressure loadings, such as applied by adaptive pressure actuators, the modeling and formulation of fluid–structure interaction can be major difficulties.

In topology optimization for structures with fluid–structure interaction, the challenges are (Hammer and Olhoff 2000; Chen and Kikuchi 2001; Du and Olhoff 2004; Sigmund and Clausen 2007; Zhang et al. 2008; Panganiban et al. 2010; Ibhadode et al. 2020): (1) the pressure load-carrying boundary evolves iteratively with varying pressure directions and magnitudes (termed design-dependent load); (2) the sensitivity of the equivalent force vector with respect to design variables is in general difficult to determine; and (3) nonlinear structural analysis is typically required due to large deformations in a compliant mechanism. Additionally, when large deformations are included, the problem becomes more complicated due to the high impact of low density elements (Bendsoe and Sigmund 2003). Thus, although topology optimization of compliant mechanisms has been widely studied, there are a few works focusing on pressure-actuated compliant mechanisms (Chen et al. 2001; Panganiban et al. 2010; Vasista and Tong 2012, 2013; Lu and Tong 2021; Kumar et al. 2020; Kumar and Langelaar 2021, 2022; de Souza and Silva 2020), which consider the void phase as an incompressible hydrostatic fluid that transfers a pressure load

Responsible Editor: Christian Gogu

✉ Yifu Lu
yifu.lu@sydney.edu.au

[1] School of Aerospace, Mechanical and Mechatronic Engineering, The University of Sydney, Sydney, NSW 2006, Australia

from a fixed fluid region to structures. In these studies, incompressibility is considered using the mixed displacement–pressure (*u/p*) coupling formulation (Sigmund and Clausen 2007) or nonconforming finite element, by which the interface boundaries are not identified and nonlinear effects are not modeled. Level-set method has been used to address this design-dependent problem via transferring topology to mechanical model by using material-fraction approach (e.g., ersatz material model (Xia et al. 2015)) or immersed boundary approaches (e.g., extended finite element method (XFEM) (Jenkins and Maute 2016)). Recently, approaches have been introduced for modeling design-dependent pressure using the work equivalent loading approach based on finite element formulations (Lu and Tong 2021, 2024) and Darcy law to determine the flux of a fluid flow due to pressure difference in a porous medium (Kumar et al. 2020; Kumar and Langelaar 2021, 2022; Kumar 2023; Banh et al. 2024).

The substructure method, a common solution method applied in FEA for solving large-scale models, has also been employed in topology optimization to condense hierarchical structure (Fu et al. 2019; Wu et al. 2019; Liu et al. 2024, 2020), large-scale topology (Huang et al. 2023), or multi-domain (Ma et al. 2005). In this method, a structure or domain (such as an element or a periodic unit cell) is subdivided into subdomains as substructures, and the substructures are condensed to a super-element with only the exterior (boundary) nodes. Although the major advantage of the substructure method is to save storage and computational cost, it has the potential to adequately capture both geometry and physics (i.e., associated equivalent stiffness matrices and pressure load vectors) of a pressure–structure interface, which is particularly difficult but crucial in nonlinear structures. Thus, in this work, we attempt to introduce the method to solve the problem of structural topology optimization involving design-dependent pressure loading.

In this study, a novel mixed substructure topology representation is proposed first for an element with and without a fluid–structure interface. An extended moving iso-surface threshold (MIST) algorithm is then developed based on the mixed topology representation for topology optimization of a structure considering geometric and material nonlinearities and subjected to design-dependent pressure loading. In this algorithm, the mixed topology representation is implemented via super-elements with equivalent stiffness matrices and equivalent load vectors and via robust model update and interface tracking schemes. The algorithm is validated via benchmark examples and numerical studies via linear and nonlinear FEA. The method is then used to design a pressurized unit cell and its associated pressurized cellular structure (PCS) for controlling airfoil thickness variation. The optimum designs of the unit cell and the PCS are fabricated and tested under selected pressure.

2 Problem statement and mixed topology representation

2.1 Problem statement

Consider the topology optimization problem for a linear or nonlinear compliant mechanism subjected to design-dependent loading, such as quasi-static distributed fluid pressure. The problem can be stated in general as: finding the optimum topology Ω that maximizes selected output displacement subject to satisfying equilibrium equations in Ω and a constraint on material volume of Ω, or formulated as: finding Ω such that

$$\text{Max}: u_{\text{out}} = \boldsymbol{u}^{(1)\text{T}}\mathbf{K}\boldsymbol{u}^{(2)} = 2\int_{\Omega} E_{\text{med}}\, d\Omega \tag{1a}$$

$$\text{s.t.}: \begin{cases} \text{Equilibrium equations} \\ \text{Material volume constraint} \end{cases} \tag{1b, c}$$

where u_{out} denotes the output displacement(s) in specific degree(s) of freedom (DOF), $\boldsymbol{u}$ and $\mathbf{K}$ represent the global displacement vector and stiffness matrix where superscript refers to virtual (1) and real (2) load cases, E_{med} represents the mutual strain energy density.

It should be noted that the compliant mechanism problem of maximizing the output displacement, as presented in Eq. 1, can be formulated based on the total mutual strain energy calculated from real (input) and virtual (output) load cases. As detailed in (Frecker et al. 1997), the output displacement u_{out} for the real load case (superscript (2)) can be expressed via considering a virtual load case $\boldsymbol{F}^{(1)}$ comprising only one unit load at the output DOF (zero at all other DOFs), by which $u_{\text{out}} = \boldsymbol{F}^{(1)^{\text{T}}}\boldsymbol{u}^{(2)} = \boldsymbol{u}^{(1)^{\text{T}}}\mathbf{K}\boldsymbol{u}^{(2)}$ (where total mutual strain energy $= \boldsymbol{u}^{(1)^{\text{T}}}\mathbf{K}\boldsymbol{u}^{(2)}/2$).

In searching forΩ, the problem in Eq. (1) is usually solved iteratively until reaching convergence in conjunction with the finite element method (FEM). To enable this iterative solution process, it is important to develop a topology representation and update model that can adequately capture both geometry and physics (or structural response) of anΩ. One approach of defining and updating Ω is to place Ω in a static background domain Ω_0 with a fixed grid mesh, i.e., $\Omega \subseteq \Omega_0$ and $\Omega_0 = \bigcup_{e=1}^{N_e}\Omega_e$ (Ω_e denotes the domain of the eth element;$e = 1,2,\ldots,N_e$; N_e is the total number of elements). As an example, Fig. 1 schematically depicts an Ω in Ω_0 with a fixed mesh of 6×6 rectangular elements, which can be

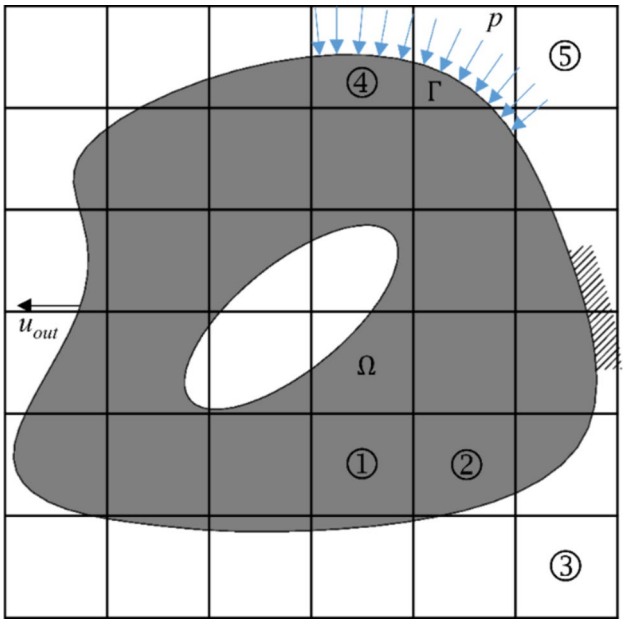

Fig. 1 An illustrative mesh for the topology optimization problem under a pressure with Ω in Ω_0

classified into three types: solid, solid–void interface and void elements (as denoted by ① , ② and ③). As a void can be filled with pressurized fluid, the solid–void interface and void elements can be further grouped as: solid–void interface elements filled partially with fluid and void elements fully filled with fluid (labeled as solid–fluid interface element ④ and void–fluid element ⑤ in Fig. 1). As both pressure magnitude and direction can be dependent of the solid–fluid interface geometry, e.g., element ④, it is important to better represent both geometry and physics of each solid–fluid interface element in every iteration for design-dependent topology optimization problems.

2.2 Mixed topology representation

A mixed substructure-density (MSD) model for topology representation and update is proposed in this section. In the MSD, all solid–fluid elements are modeled by using an interface boundary conforming substructure mesh with solid or void–fluid sub-elements, whereas all the remaining are solid, void or grey elements. As an example, Fig. 2a, d depicts a 4-node solid–fluid interface element with a distributed pressure, which is modeled with a simple or complex interface-conforming substructure meshing in Fig. 2b, e, $\Omega_e = \bigcup_{k=1}^{N_{\text{sub}}} \Omega_{ek}$ (where Ω_{ek} is the subdomain of the kth sub-element; N_{sub} denotes the total number of sub-elements) and then physically represented by a 4-node element with equivalent stiffness or tangential stiffness matrix $\mathbf{K}_e^*$ and equivalent nodal force vector $\mathbf{F}_e^*$ statically condensed as shown in Fig. 2c.

Figure 3 depicts an illustrative example of using the MSD mixed substructure topology representation on the structural level. In MSD, the crisp boundary of topology Ω can captured collectively by that of each interface element, and the associated physics can be represented by solving equilibrium Eq. (1b) in conjunction with super-elements with $\mathbf{K}_e^*$ and $\mathbf{F}_e^*$ for linear and nonlinear cases.

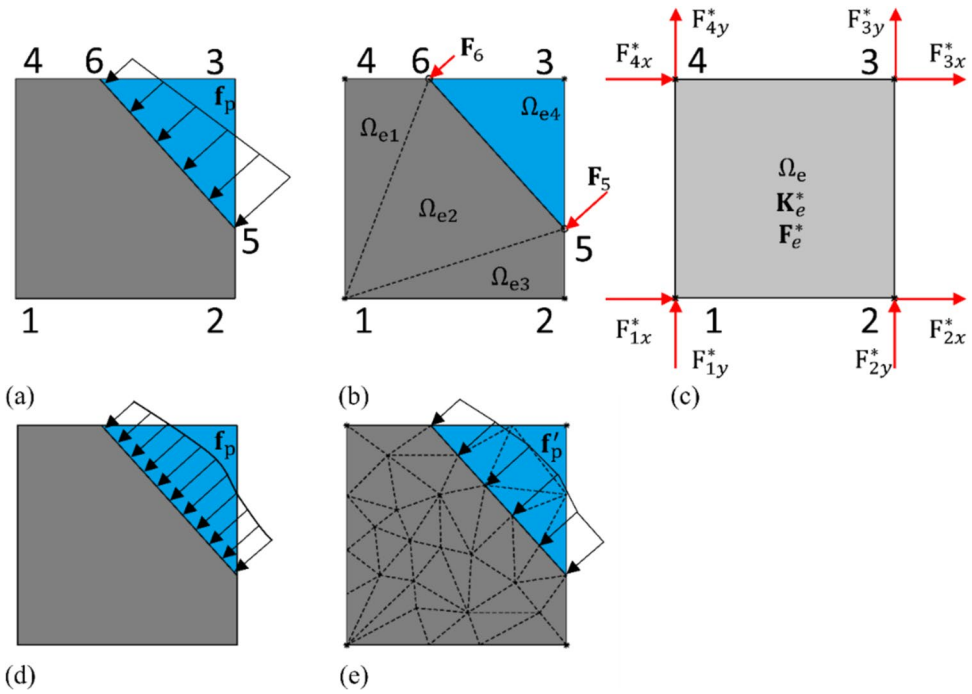

Fig. 2 Schematics of substructure representations of 4-node solid–fluid interface element subjected to: **a** linearly distributed or **d** non-uniform pressure, with a simple (**b**) and complex **e** interface-conforming substructure meshing, and (c) their equivalent element

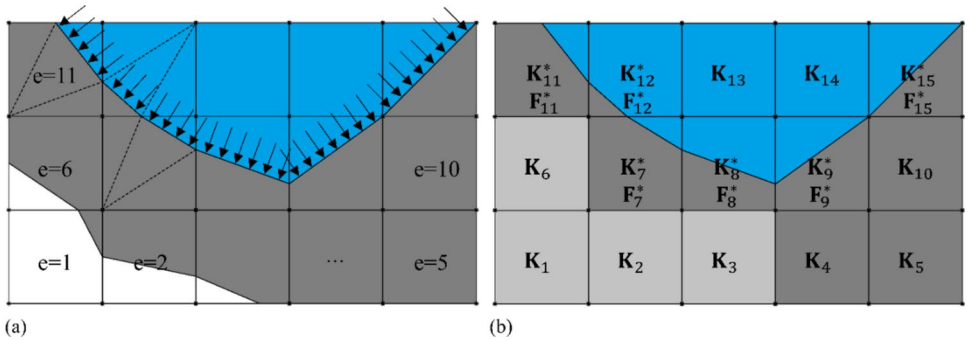

Fig. 3 Mixed topology representation of a solid–fluid interface with pressure loading (**a**) and its condensed FE model (**b**)

2.2.1 Linear case

For a linear case, the material properties for all solid and void–fluid sub-elements in a solid–fluid element in MSD are given by:

$$\mathbf{D}_{\text{solid}} = \mathbf{D}_0;\ \mathbf{D}_{\text{void}} = \mathbf{D}_{\text{fluid}} = x_{\min}^p \mathbf{D}_0 \tag{2a}$$

where $\mathbf{D}_0$ represents the pristine material property matrix; x_e ($x_{\min} < x_e < 1$) denotes the area ratio of the solid portion-to-entire element and p is a penalty factor as used in SIMP (Bendsoe and Sigmund 2003); $x_{\min}$ is a small number ($= 10^{-3}$) to enable the inclusion of a void or void–fluid element or sub-element in FEA without causing singularity. The material property for each of the non-solid–fluid elements is assumed to be

$$\mathbf{D}_{\text{g}} = x_e^p \mathbf{D}_0 \tag{2b}$$

In this case, equilibrium Eq. (1b) becomes:

$$\mathbf{K}\mathbf{u} = \mathbf{F} \tag{3a}$$

where

$$\mathbf{K} = \sum_{e=1}^{N_{se}} \mathbf{K}_e^* \oplus \sum_{e=N_{se}+1}^{N_e} \mathbf{K}_e;\quad \mathbf{F} = \sum_{e=1}^{N_{se}} \mathbf{F}_e^* \oplus \sum_{e=N_{se}+1}^{N_e} \mathbf{F}_e \tag{3b}$$

and e denotes the eth element and the operator $\oplus$ represents global matrix assemblage; N_{se} represents the total number of the solid–fluid interface elements; and $\mathbf{K}_e$, $\mathbf{K}_e^*$, $\mathbf{F}_e$ and $\mathbf{F}_e^*$ (superscript $*$ refers to substructures, e.g., a super-element as depicted in Figs. 2c and 3b) are given by:

$$\mathbf{K}_e = x_e^{\text{p}} \int_{\Omega_{\text{e}}} \mathbf{B}^{\mathbf{T}} \mathbf{D}_0 \mathbf{B} d\Omega_{\text{e}} \tag{4}$$

$$\mathbf{K}_e^* = [\mathbf{K}_{oo}] - [\mathbf{K}_{oi}][\mathbf{K}_{ii}]^{-1}[\mathbf{K}_{io}];\quad \mathbf{F}_e^* = \{\mathbf{F}_o\} - [\mathbf{K}_{oi}][\mathbf{K}_{ii}]^{-1}\{\mathbf{F}_i\} \tag{5}$$

where $\mathbf{B}$ is the strain–displacement matrix, and Eq. (5) can be determined from $\delta U_{\text{e}} = \delta W_{\text{e}}$ using Eqs. (6–7)

$$\delta U_{\text{e}} = \int_{\Omega_{\text{e}}} \delta\boldsymbol{\varepsilon}^{\text{T}} \boldsymbol{\sigma} d\Omega_{\text{e}} = \left\{ \delta\mathbf{u}_o^T \ \delta\mathbf{u}_i^T \right\} \begin{bmatrix} \mathbf{K}_{oo} & \mathbf{K}_{oi} \\ \mathbf{K}_{io} & \mathbf{K}_{ii} \end{bmatrix} \begin{Bmatrix} \boldsymbol{u}_o \\ \boldsymbol{u}_i \end{Bmatrix} \tag{6}$$

$$\delta W_{\text{e}} = \int_{\Gamma_{\text{e}}} \delta\boldsymbol{u}^{\text{T}} \mathbf{f}_{\text{p}} d\Gamma_{\text{e}} = \sum_{k=1}^{N_{sub}} \int_{\Gamma_{\text{ek}}} \delta\boldsymbol{u}^{\text{T}} \mathbf{f}_{\text{p}} d\Gamma_{\text{ek}} = \left\{ \delta\mathbf{u}_o^T \ \delta\mathbf{u}_i^T \right\} \begin{Bmatrix} \mathbf{F}_o \\ \mathbf{F}_i \end{Bmatrix} \tag{7}$$

where $\mathbf{K}_{oo}$, $\boldsymbol{u}_o$, and $\mathbf{F}_o$ are the stiffness matrix, displacement, and force vectors for the exterior DOFs; $\mathbf{K}_{ii}$, $\boldsymbol{u}_i$, and $\mathbf{F}_i$ are those for the interior DOFs;$\mathbf{K}_{oi}(= \mathbf{K}_{oi}^{\text{T}})$ is the coupling stiffness; N_{sub} is the total number of sub-elements; Γ_e denotes the interface boundary of the eth element Ω_e; and Γ_{ek} is the boundary of the kth sub-element Ω_{ek}.

2.2.2 Nonlinear case

For the case of material nonlinearity, the properties of solid and void/void–fluid sub-elements in any solid–fluid element are assumed to be:

$$\sigma_{\text{solid}} = \sigma(\varepsilon);\quad \sigma_{\text{void}} = \sigma_{\text{fluid}} = x_{\min}^p \sigma(\varepsilon) \tag{8}$$

where $\sigma(\varepsilon)$ denotes the prescribed stress–strain relationships of the solid material, which can be tabulated for data input in nonlinear finite element analysis (NFEA). The nonlinear material property for any non-solid–fluid interface element is assumed to be:

$$\sigma_e = x_e^p \sigma(\varepsilon) \tag{9}$$

In NFEA, all external loads are usually applied incrementally to a structure via M load steps: ${}^{\tau}\mathbf{F}(\tau = 1,2,\ldots,M)$. By using the total Lagrangian formulation, equilibrium Eq. (1b) at load step $\tau+1$ can be broadly expressed as (Bathe 1996; Luo and Tong 2016):

$$\mathbf{K}^{\tau} \Delta\mathbf{u}^{\tau+1} = \mathbf{F}^{\tau+1}\ (= 0,1,2,\ldots,M-1) \tag{10}$$

where

$$\mathbf{K}^{\tau} = {}_0^{\tau}\mathbf{K}_L + {}_0^{\tau}\mathbf{K}_{NL};\Delta\mathbf{u}^{\tau+1} = {}^{\tau+1}\mathbf{u} - {}^{\tau}\mathbf{u};\mathbf{F}^{\tau+1} = {}^{\tau+1}\mathbf{F} - {}_0^{\tau}\mathbf{F}_r \tag{11a}$$

$$ {}_0^{\tau}\mathbf{K}_L = \sum_{e=1}^{N_{se}} {}_0^{\tau}\mathbf{K}_{Le}^{*} \oplus \sum_{e=N_{se}+1}^{N_e} {}_0^{\tau}\mathbf{K}_{Le} ; {}_0^{\tau}\mathbf{K}_{NL} = \sum_{e=1}^{N_{se}} {}_0^{\tau}\mathbf{K}_{NLe}^{*} \oplus \sum_{e=N_{se}+1}^{N_e} {}_0^{\tau}\mathbf{K}_{NLe} \tag{11b} $$

$$ {}^{\tau+1}\mathbf{F} = \sum_{e=1}^{N_{se}} {}^{\tau+1}\mathbf{F}_e^{*} \oplus \sum_{e=N_{se}+1}^{N_e} {}^{\tau+1}\mathbf{F}_e ; {}_0^{\tau}\mathbf{F}_r = \sum_{e=1}^{N_{se}} {}_0^{\tau}\mathbf{F}_{re}^{*} \oplus \sum_{e=N_{se}+1}^{N_e} {}_0^{\tau}\mathbf{F}_{re} \tag{11c} $$

and ${}^{\tau}\mathbf{u}$ and ${}^{\tau+1}\mathbf{u}$ represent the nodal displacement vector at load steps τ and $\tau+1$; ${}_0^{\tau}\mathbf{K}_L$, ${}_0^{\tau}\mathbf{K}_{Le}^{*}$, ${}_0^{\tau}\mathbf{K}_{Le}$, ${}_0^{\tau}\mathbf{K}_{NL}$, ${}_0^{\tau}\mathbf{K}_{NLe}^{*}$ and ${}_0^{\tau}\mathbf{K}_{NLe}$ are the global or element linear and nonlinear strain incremental stiffness matrices formulated for the non-deformed whole structure, interface or non-interface element at load step τ; ${}^{\tau+1}\mathbf{F}$, ${}^{\tau+1}\mathbf{F}_e^{*}$ and ${}^{\tau+1}\mathbf{F}_e$ are the global or element external load vectors applied to the non-deformed whole structure, interface or non-interface element at load step $(\tau+1)$; ${}_0^{\tau}\mathbf{F}_r$, ${}_0^{\tau}\mathbf{F}_{re}^{*}$ and ${}_0^{\tau}\mathbf{F}_{re}$ denote the global or element nodal stress resultant vector determined using the non-deformed structure, interface and non-interface element at load step τ (see Bathe 1996; Luo and Tong 2016) for details); the right superscript $*$ refers to the quantities statically condensed similar to Eqs. (5–7); and the left subscript 0 refers to the non-deformed domain.

It should be noted that, similar to Eq. (3b), ${}_0^{\tau}\mathbf{K}_{Le}^{*}$, ${}_0^{\tau}\mathbf{K}_{NLe}^{*}$, ${}^{\tau+1}\mathbf{F}_e^{*}$ and ${}_0^{\tau}\mathbf{F}_{re}^{*}$ in Eq. (11b,c) are the equivalent matrices and vectors statically condensed for a solid–fluid interface element; and such element-based static condensation for eliminating interior DOFs needs to be conducted in each of the M load steps. In addition, Eq. (10) for each load step is typically solved for a number of iterations depending on the choice of solver and its parameters.

3 Formulation and algorithm

In this work, an extended MIST algorithm is proposed to implement topology optimization under design-dependent pressure loading and considering geometric and material nonlinearities, based on the mixed topology representation and substructure method (see Sect. 2.2). In this section, the optimization problem as formulated in Eq. (1) is first re-formulated using the MIST method, and then numerically implemented.

3.1 Formulation

In the MIST method (Tong and Lin 2011; Vasista and Tong 2014), the objective function and constraint are expressed in the form of convolutional integrals. The problem in Eq. (1) can be formulated as: find Ω that

$$ \max : u_{\text{out}} = \int_{\Omega_0} \Phi H(\Phi - t) d\Omega \tag{12a} $$

$$ \text{s.t.} : \begin{cases} \mathbf{K}^{(l)}\mathbf{u}^{(l)} = \mathbf{F}^{(l)} \text{ or } \mathbf{K}^{(l)\tau}\Delta\mathbf{u}^{(l)\tau+1} = \mathbf{F}^{(l)\tau+1} (l = 1, 2; = 0, 1, 2, \ldots, M-1) \\ \int_{\Omega_0} H(\Phi - t) d\Omega \le V_f V_0 \end{cases} \tag{12b, c} $$

where Φ is the spatial function in Ω_0 related to structural responses and solutions of Eq. (12b); $H(\Phi - t)$ is the Heaviside function and t is an iso-surface threshold; superscript l refers to virtual ($l = 1$) and real ($l = 2$) load; superscript τ refers to the synchronized load step $\mathbf{F}^{(l)\tau} = {}^{\tau}\Delta\mathbf{F}^{(l)}$ (where ${}^{\tau}\Delta$ is a load factor and $0 = {}^{0}\Delta < {}^{1}\Delta < {}^{2}\Delta < \ldots {}^{\tau}\Delta < \cdots < {}^{M-1}\Delta < {}^{M}\Delta = 1$); and V_f and V_0 denote the prescribed volume fraction and the total volume of Ω_0 and u_{out} denotes $u_{out}^{(2)}$ for the linear case and the displacement at the full real load ${}^{M}u_{out}^{(2)}$ for nonlinear case. It is worth noting that Eq. (12b) can also be presented in the form of integrals over Ω_0 (Bathe 1996).

3.1.1 Response function

In the MIST method, a physical response function is applied to update design variables and topologies. The objective function needs to be rewritten in an integral form as in Eq. (12a), and the response function should be derived based on the integrand. Thus, the response function indicates the relative nodal physical performances with respect to the objective function and serves as the sensitivity information for the topology updates, by which explicit sensitivity analysis is not necessary.

For the compliant mechanism problem, by using the virtual work principle, the objective function (output displacement u_{out}) can be written as the total mutual strain energy. As in Eq. (1a), the mutual strain energy density is the integrand function of the integral and thus can be used as a response function or part of it. To circumvent discontinuity on the load-carrying surface, one can also add strain energy density as part of the response function. Thus, based on the FE solution of the kth iteration, the response function Φ can be chosen as:

$$ \Phi^k = \overline{\Phi}^k, \quad \text{for k} = 1 \tag{13a} $$

$$ \Phi^k = \left(1 - k_\Phi\right)\overline{\Phi}^{k-1} + k_\Phi \overline{\Phi}^k, \quad \text{for } k \ge 2 \tag{13b} $$

where

$$ \overline{\Phi}^k = (1 - \alpha)E_{\text{med}}^k + \alpha E_{\text{sed}}^k \quad (k = 1, 2, \ldots) \tag{14} $$

where α and k_Φ are two user-defined coefficients ($0 \le \alpha \le 1$; $0 < k_\Phi \le 1$; $k_\Phi \ne 1$ and/or $\alpha \ne 0$ should be used to

circumvent discontinuity on the load-carrying surface); ${E_{med}}^{k}$ and E_{sed}^{k} can be determined for the kth FE model as follows.

The mutual strain energy density E_{med} in Eq. (14) can be determined by using the principle of virtual work in conjunction with the solutions of Eq. (12b) for an FE model. Let us denote: (i) $\mathbf{u}^{(l)}$, $\boldsymbol{\varepsilon}^{(l)}$ and $\boldsymbol{\sigma}^{(l)}(l = 1,2)$ as the linear displacement, strain and stress; and (ii) ${}^{\tau}\mathbf{u}^{(l)}$, ${}^{\tau}\boldsymbol{\varepsilon}^{(l)}$ and ${}^{\tau}\mathbf{S}^{(l)}$ $(\tau = 1,2,\ldots,M; l = 1,2)$ as the nonlinear displacement, Green–Lagrange strain and Piola–Kirchhoff stress at the τ^{th} synchronized load step $\mathbf{F}^{(l)\tau} = {}^{\tau}\Delta\mathbf{F}^{(l)}$. Let $\mathbf{F}^{(1)} = \mathbf{f}^{(1)}$ for linear case or $= f^s\mathbf{f}^{(1)}$ for nonlinear case (where $\mathbf{f}^{(1)}$ is a unit virtual load in relation to u_{out} in Eq. (1a)), by using the principle of virtual work (see details for the nonlinear case in Appendix), one can determine E_{med} as follows:

$$\text{(i)Linear}: \quad E_{\text{med}} = \frac{1}{2}\boldsymbol{\sigma}^{(1)T}\boldsymbol{\varepsilon}^{(2)} \tag{15}$$

$$\text{(ii)Nonlinear}: E_{\text{med}} = \sum_{\tau=1}^{M}\frac{1}{2}\left(\frac{{}^{\tau}\mathbf{S}^{(1)T} + {}^{\tau-1}\mathbf{S}^{(1)T}}{\left({}^{\tau}\Delta + {}^{\tau-1}\Delta\right)f^s}\right)\left({}^{\tau}\boldsymbol{\varepsilon}^{(2)} - {}^{\tau-1}\boldsymbol{\varepsilon}^{(2)}\right) \tag{16}$$

Equation (16) formulates the nonlinear mutual strain energy density using trapezium area sums for all load steps. In practice, it could be approximated using the mutual strain energy at the final state only (Jung and Gea 2004; Bruns and Tortorelli 2001). In the present formulation, Eq. (16) can be further approximated using only one segment from load step $\tau =$ 0 to M. In this case, Eq. (16) is approximated by using only the strain ${}^{M}\boldsymbol{\varepsilon}^{(2)}$ and stress ${}^{M}\mathbf{S}^{(1)}$ at the final state in NFEA:

$$E_{\text{med}} = {}^{M}\mathbf{S}^{(1)TM}\boldsymbol{\varepsilon}^{(2)}/2f^s \tag{17}$$

In addition, one can also calculate the strain energy density for the real load via

$$E_{\text{sed}} = \begin{cases} \boldsymbol{\sigma}^{(2)T}\boldsymbol{\varepsilon}^{(2)}/2 \text{ for linear} \\ {}^{M}\mathbf{S}^{(2)TM}\boldsymbol{\varepsilon}^{(2)}/2f^s \text{ for nonlinear} \end{cases} \tag{18}$$

It is noted that the unit virtual force $\mathbf{f}^{(1)}$ applied to the output port may be so high that the NFEA diverges or too low to have nonlinear effects. Thus, in the nonlinear case, the magnitude of the virtual force f^s may not be unit one and needs to be carefully determined. In practice, it could be determined via a trial-and-error approach, in which the load is selected as a percentage (e.g., 90%) of the lowest load to diverge NFEA.

3.1.2 Solution procedures

In MIST (Tong and Lin 2011; Vasista and Tong 2014), the problem in Eq. (12) can be solved iteratively via the following steps: (a) initialize/create FE model for (12b); (b) solve Eq. (12b); (c) determine function Φ and generate new topology; (d) update FE model; and (e) repeat (b)–(d) until converged. Hence, it is necessary to elaborate on the determination of function Φ and update of FE model.

Topology Ω^k and its area ratio $\left(\overline{x_e^k}\right)$ can be obtained by using Φ^k via solving Eq. (12a,c) and finding t^k. Combining $\overline{x_e^k}$ with x_e^{k-1} yields the following updated x_e^k

$$x_e^k = \max\left\{\left(x_e^{k-1}\right) + k_{mv}\left[\left(\overline{x_e^k}\right) - \left(x_e^{k-1}\right)\right], x_{\min}\right\} \quad (e = 1,2,\ldots,N_e) \tag{19a}$$

where k_{mv} $(0 < k_{mv} \le 1)$ is a move limit and x_e^0 is an initial design. Once x_e^k is determined, one can update the FE model via Eqs. (2), (8) and (9). It is worth noting that some void and void-fluid elements can be removed from NFEA (Luo and Tong 2016) via:

$$x_e^k = 0 \quad \text{if } x_e^k \le \varepsilon \tag{19b}$$

where ε is a small constant (typically chosen to be equal to $x_{\min}$).

In the present MSD-based FE model update scheme, the modified algorithm goes: (i) calculate x_e^k via Eq. (19) and store x_e^k for all element Ω_e^k; (ii) for every solid–fluid interface element Ω_e^k, create a super-element in Ω_e^k (to replace the element or super-element Ω_e^{k-1} in the previous iteration); and (iii) for all the remaining elements Ω_e^k, use x_e^k to update its material input via Eq. (2) (linear) or (8,9) (nonlinear). The second step is novel, and it enables enhanced modeling of the crisp and pressurized solid–fluid interface boundary via the relevant equivalent element stiffness matrix and load vector.

The solid–fluid interface or elements in Ω^k can be tracked by using a fluid flooding scheme (Chen and Kikuchi 2001; Picelli et al. 2019). In this scheme, fixed (non-design) fluid regions are pre-defined in initialization, and all elements that neighbor or overlap with either fluid or solid–fluid interface elements are classified as: (a) a fluid element if $\left(\overline{x_e^k}\right) \le 20x_{\min}$; (b) a solid–fluid interface element if $20x_{\min} < \left(\overline{x_e^k}\right) < 0.98$; and (c) a solid element if $\left(\overline{x_e^k}\right) \ge 0.98$. This classification propagates (like flooding) until no additional fluid or solid–fluid interface element can be identified. In the subsequent iteration, a reclassification and identification will be initiated from the same pre-defined fluid region(s). It should be noted that the parameters for classifying fluid and solid elements are chosen to be $20x_{\min}$ and 0.98 instead of $x_{\min}$ and 1. These parameters was chosen to avoid very high aspect ratios of sub-elements in super-elements and to avoid duplicated nodes created by too small clearances in substructures.

3.2 Algorithm

An extended MIST algorithm is developed to solve the problem in Eq. (12). It is important to note that a powerful nonlinear NFEA solver is crucial as Eq. (12b) can be highly nonlinear due to the presence of elements with extremely low stiffness or $x_{\min}$ (Yoon and Kim 2007; Bandi et al. 2011; Luo and Tong 2016). In this work, the MIST algorithm is coded in MATLAB and interfaced with NASTRAN as the NFEA solver. The FEA data file is generated through programming in MATLAB, solved in NASTRAN, and the FEA result files are processed using the textscan function in MATLAB to extract the necessary data. For the basic MIST algorithm and more details of interface with NASTRAN, please refer to (Tong and Lin 2011; Luo and Tong 2016). The main additional features of the present extended MIST consist of the use of MSD, solid–fluid interface tracking scheme, and MSD-based update scheme of FE model. The extended algorithm interfaced with Nastran goes as follows:

Step 1: Initialization.

- Input: α, k_Φ, $x_{\min}$, V_f and k_{mv}
- Initialize: $\boldsymbol{x}_e^0$ (define non-design fluid and solid region, and $\boldsymbol{x}_e^0 = V_f$ for other elements, i.e., material evenly distributed), and FE model in Ω_0

Step 2: FEA/NFEA solution.

Solve Eq. (12b) for the kth FE model.

- Step 3: Determination of function Φ^k and topology Ω^k
  - Calculate nodal Φ^k via Eqs. (13, 14) and construct Φ^k function including filtering
  - Solve Eq. (12c) and find the iso-surface level t^k with respect to V_f via bisection method
  - Determine topology Ω^k and its area ratio $\left(\overline{\boldsymbol{x}_e^k}\right)$
  - Identify solid–fluid elements Ω_{e}^k and its interface $\Gamma_{\mathrm{e}}^{\mathrm{k}}$ using the fluid flooding method and $\left(\overline{\boldsymbol{x}_e^k}\right)$
- Step 4: Update of FE model using MSD.
  - Calculate and retain $\boldsymbol{x}_e^k$ using Eq. (19)
  - Update material input using Eq. (2) or (8,9) and $\boldsymbol{x}_e^k$ for all non-solid–fluid elements
  - Construct super-elements using Ω_{e}^k and $\Gamma_{\mathrm{e}}^{\mathrm{k}}$ for all solid–fluid interface elements
- Step 5: Convergence check.

  Calculate convergence parameter (Luo and Tong 2016):

$$\Delta\Phi^k = \frac{1}{V_f N_n}\left[\sum_{r_n=1}^{N_n}\left|\Phi^k(r_n) - \Phi^{k-1}(r_n)\right|\right] \tag{20}$$

where $\Phi^k(r_n)$ is the Φ value at node r_n and N_n is the total number of nodes;

If $\Delta\Phi^k < \varepsilon_c$ (ε_c is small constant) and/or the maximum iteration number is reached, terminate the iteration; otherwise, go to Step 2 and repeat.

4 Numerical examples

In this section, benchmark examples, an internally pressurized lid and a pressurized bending unit cell, are presented to validate the present algorithm. In addition, due to the presence of artificial springs, full FEAs are conducted for the optimized topologies to verify their deformation and shape-changing performance.

4.1 Internally pressurized lid

Figure 4a depicts the design domain, material properties, and dimensions of this minimum compliance problem subjected to pressure loading, which is a representative

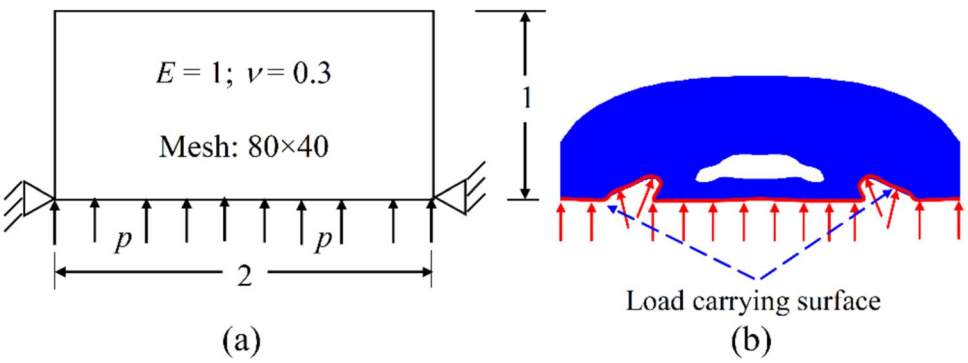

Fig. 4 An internally pressurized lid **a** design domain, material properties and dimensions of an internally pressurized lid where pressure $p = 1$; **b** topology and load-carrying surface at iteration 5 ($k = 5$) in the present computation for the results of column 1 in Fig. 5

example of design-dependent loading problems and has been investigated by many researchers (Chen and Kikuchi 2001; Du and Olhoff 2004; Sigmund and Clausen 2007; Zhang et al. 2008; Panganiban et al. 2010; Picelli et al. 2015; Jiang and Zhao 2020). Figure 4b illustrates an example of the load-carrying surface in an iteration of the present algorithm. To compare with those available results, only the linear problem is considered. For the minimum compliance problem, we choose $\Phi = E_{sed}$ (defined in Eq. (18)) and $\alpha = 1$ in Eq. (14) to adapt the problem formulation in Eq. (12).

Figure 5 depicts the material distributions at iterations 1 (initialization), 10, 50 and 100, and the optimized topologies ($k = 100$) for $V_f = 0.5$ with different material initializations and different k_Φ. The objective function and topology converge after 70 iterations for all cases, although slightly better numerical stability can be achieved by using a combined response function with $k_\Phi \neq 1$. However, this may not be necessary as the topologies in Fig. 5 are almost the same for different values of k_Φ including $k_\Phi = 1$ in the minimum compliance problem.

The optimized topologies in Fig. 5 correlate well with those presented in (Chen and Kikuchi 2001; Du and Olhoff 2004; Sigmund and Clausen 2007; Zhang et al. 2008; Panganiban et al. 2010; Picelli et al. 2015; Jiang and Zhao 2020). The converged strain energy in the present study is $E_{se} = 3.48$–3.87 for $V_f = 0.5$, which is comparable to the compliance numerically integrated along the loading surface in the literature, i.e. $E_{se} = 4.7$–5.6 (Sigmund and Clausen 2007); $E_{se} = 6.1$ (Zhang et al. 2008); and $E_{se} = 4.57$–4.71 (Panganiban et al. 2010). The discrepancies could be due to the differences in calculating strain energy and compliance, and in the load-carrying surface, e.g., the present height h in Fig. 5 is slightly larger. In addition, all the void elements are kept ($x_e = 10^{-3}$) in (Sigmund and Clausen 2007; Zhang et al. 2008; Panganiban et al. 2010), but they are removed in the present study. Evidently, the present optimum topologies and the objective functions correlate fairly well with those in the literature, which validates the present algorithm.

4.2 Pressurized bending unit cell

Figure 6a depicts the computational model for a half of the unit cell with dimensions, load, and boundary conditions and solid and fluid non-design regions. The objective is to generate bending deformation along the right side via maximizing $u_{\text{out1}} - u_{\text{out2}}$. This problem is investigated with two design cases being considered: 1) case I with real load $p = 1$ and virtual load $\mathbf{F}^{(1)}$ consisting of two unit dummy load $F_{\text{out1}} = 1$ and $F_{\text{out2}} = -1$, which is taken from the literature (Vasista and Tong 2012) for validation and benchmark purposes, using the linear MSD; and case II with real load $p = 0.01$ and virtual load $\mathbf{F}^{(1)}$ consisting of two loads $F_{\text{out1}} = 2$ and $F_{\text{out2}} = -2$ for the linear and nonlinear MSD. As the virtual and real unit loads from the literature (case I) are either too high that the NFEA diverges or too low to have nonlinear effects, those loads, as well as the coupled artificial spring stiffness, are reconsidered and selected for the geometrical nonlinear designs as case II via a trial-and-error approach. For example, if the virtual load $\mathbf{F}^{(1)}$ is two unit dummy loads, the resulting displacements are too small to exhibit nonlinear effects; when $\mathbf{F}^{(1)}$ is $F_{\text{out1}} = 2.25$ and $F_{\text{out2}} = -2.25$, the NFEA diverged; and $90\% \times \mathbf{F}^{(1)}$ ($F_{\text{out1}} = 2$ and $F_{\text{out2}} = -2$) is then tested and yields converged results, which is therefore selected.

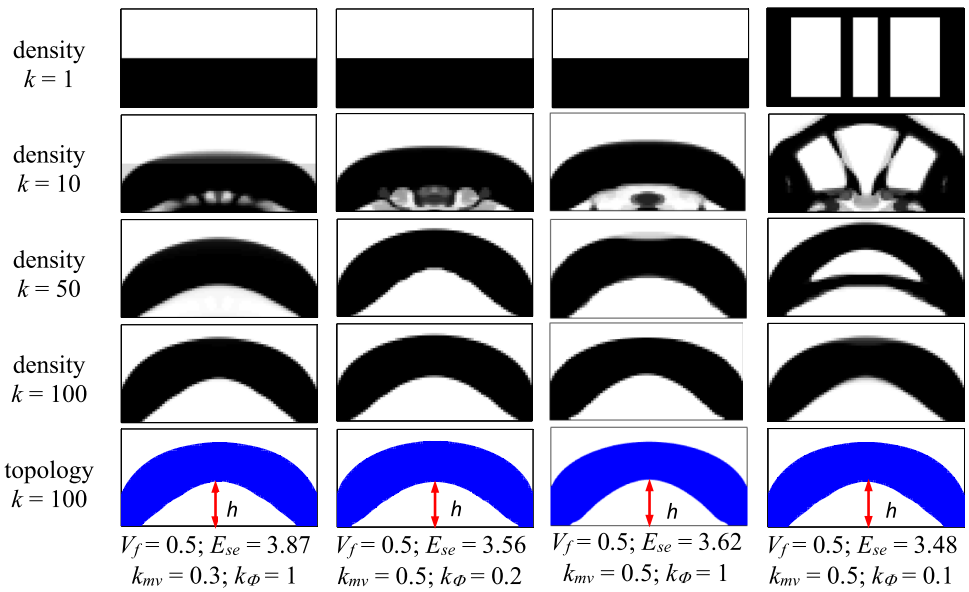

Fig. 5 Material distributions and optimized topologies of an internally pressurized lid in linear analysis for different volume fractions and initializations

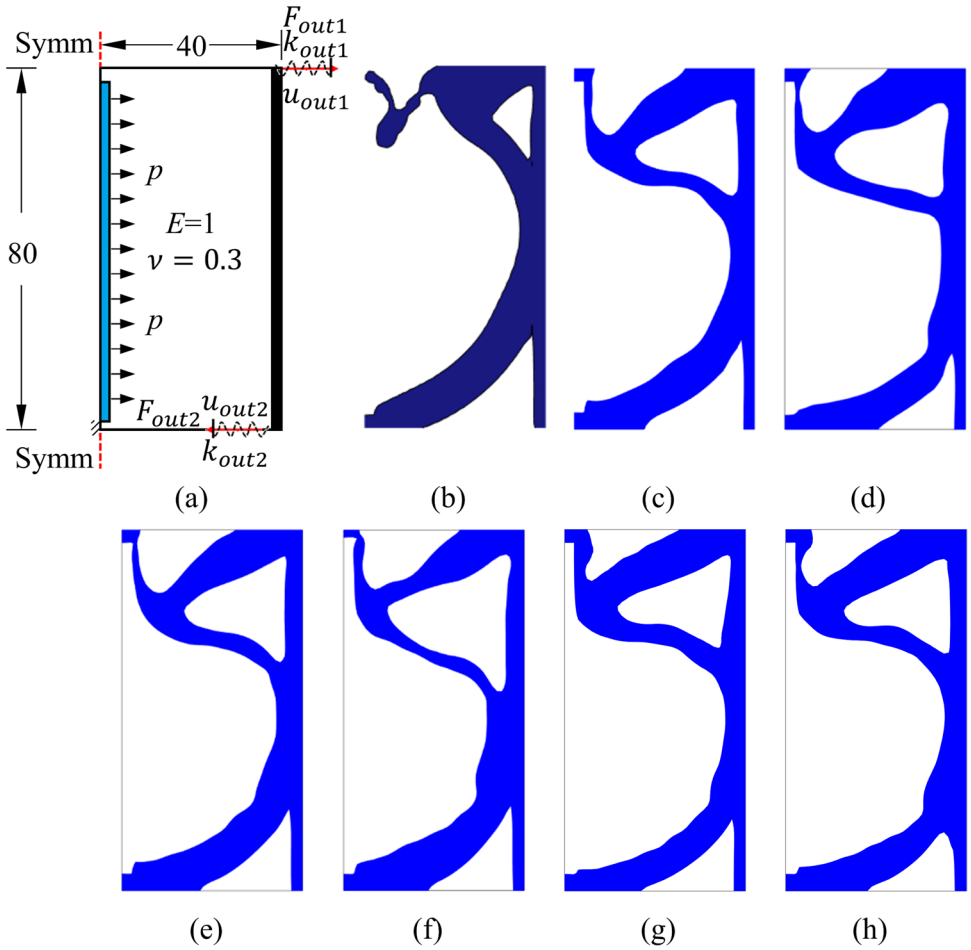

Fig. 6 Bending unit cell design: **a** design domain; the optimum topologies for case I by using **b** the *u/p* formulation in (Vasista and Tong 2012), **c** the equivalent loading method in (Lu and Tong 2021), and **d** the present linear MSD; the optimum topologies for case II by using the present **e** linear and **f** nonlinear MSD. **g** and **h** different material penalty schemes of case II linear (**e**)

The material properties, $E = 1$ and $\upsilon = 0.3$, are equivalent to the shear and bulk modulus used in (Vasista and Tong 2012). The spring stiffness $k_{\text{out1}} = k_{\text{out2}} = 0.5$ from (Vasista and Tong 2012) are used. In the present computation, $k^0_{\text{mv}} = 0.3$ is initialized and halved when oscillation occurs until reaching $k^0_{\text{mv}}/2^4$ for the linear cases and $k^0_{\text{mv}}/2^6$ for the nonlinear cases; filter radius $r_{\text{min}} = 3$ (3 times of element size); and $k_\Phi = 0.5$ and $\alpha = 0.3$. The material penalty should have been selected as $p = 3$ by using the SIMP scheme. However, $p = 3$ will cause the low density elements to exhibit extremely large deformations at the early iterations, which may diverge the NFEA or result in discontinuities and islands on the pressure-structure interfaces. Thus, the material penalty is initialized as 1 and increases to 3 by a relatively fast 0.05 increment per iteration, ensuring sufficient time/iterations for the topologies to converge for $p = 3$. For nonlinear topology optimization problems, it is common to use a continuation method to control the penalty parameter p. In the literature, two methods have been considered: (1) allow the problem to converge for each increased p until $p = 3$ is reached (Buhl et al. 2000); and (2) use an iteratively incrementing penalty parameter p until $p = 3$ (Bruns and Tortorelli 2001). In this work, method (2) is chosen to prevent premature convergence of the pressure–structure interface for design-dependent loading problems.

Parameter k_Φ is used to avoid large fluctuation of the Φ function and α is to circumvent discontinuities on load-carrying surfaces. α should be as small as possible to achieve the optimal compliant mechanism designs and sufficiently large to prevent discontinuities on interface boundaries. When 0.05, the load-carrying surface is separated in iteration even if k is very small ($k < 0.05$). Thus, $\alpha = 0.3$ and $k = 0.5$ are selected in this study.

Figure 6b, c, d depict the optimum topologies for linear design case I obtained respectively by using the *u/p* formulation in (Vasista and Tong 2012), the work equivalent lng method in (Lu and Tong 2021), and the present linear MSD. As shown in Fig. 6b, d, the optimum topology obtained using the present linear MSD and the *u/p* formulation in (Vasista and Tong 2012) are comparable and similar, with a main difference in the upper half of the unit cell. The optimized objective function obj $= u_{\text{out1}} - u_{\text{out2}}$ predicted by the present linear MSD is 51.39, which is 33.6% larger than that (38.46) obtained in (Vasista and Tong 2012). Moreover, the optimized topology using the present linear MSD is also very similar to that obtained via the equivalent loading method

in (Lu and Tong 2021) (see Fig. 6c, d), while the objective function is 9.67% larger compared to the equivalent loading method (46.86). However, it is worth noting that these significant increases in the output displacements come at a cost because the output displacements are obtained via ~ 100 iterations using the present MSD method, ~ 80 iterations using the work equivalent loading method, and ~ 30 iterations using the *u/p* method.

Figure 6f depicts the optimum topologies for design case II obtained by using the present nonlinear MSD to illustrate the influence of geometrical nonlinearity, while the linear MSD with identical settings is studied as comparisons (Fig. 6e). The topologies in Fig. 6c–e appear to resemble each other although there exist differences in size and shape details. Figure 7 shows the associated convergence histories of the objective function for the present linear and nonlinear MSD for design case II, respectively. Since the load-carrying boundary evolves during iterations, which is reflected by an element switching between fluid (a homogeneous ersatz material) and solid–fluid (a condensed super-element) in the present MSD topology representation, some oscillations can be observed during iterations for both linear and nonlinear cases, even though k_{Φ} is employed. It is observed that the nonlinear case (red curve) is less stable than the linear case (black curve) due to the inherent nature of nonlinear problems. Numerical instabilities in nonlinear problems include: the divergence of the NFEA may be caused by the low density elements (as the tangent stiffness matrix can become indefinite or negative definite as a result of large displacements); divergence or non-convergence of the optimization algorithm; premature convergence of the optimization algorithm, etc. Correspondingly, low density elements are removed; a significantly smaller move limit k_{mv} is selected in the nonlinear case compared to the linear case; a relatively fast 0.05 increment is applied to control the penalty parameter p. However, the oscillation amplitude remains relatively larger than the linear case. The converged objective function obj $= u_{\mathrm{out1}} - u_{\mathrm{out2}}$ is 1.22 for the nonlinear case, which is slightly larger than 1.18 for the linear case.

In addition, the effects of material penalty schemes are also studied. Figure 6g, h shows the topologies for case II with linear MSD and material penalties of $p = p + 0.067$ (reaching $p = 3$ faster than in Fig. 6e) and $p = p + 0.04$ (reaching $p = 3$ slower). In Fig. 6g, the rapid increase in p results in weak stability and failure to achieve convergence, although the objective function value at iteration 100 $obj = 1.39$ is higher than that of the recommended penalty scheme in Fig. 6e. By contrast, the slower increase in Fig. 6h ensures stability, but the objective function value of 1.15 is lower than that in Fig. 6e. Therefore, the increment of the material penalty should be selected within a certain range, avoiding both too fast and too slow increases. In addition, an alternative scheme to control the material penalty is also considered, where the penalty p is increased by 0.05 every 5 iterations until $p = 3$, allowing the problem to converge for each increased p. The optimized objective function, obj = 1.20, is lower than the result obtained with the selected setting obj = 1.22. The possible cause could be premature convergence of the pressure–structure interface.

Full linear FEAs are conducted for the three optimized linear designs in Fig. 6b, c, d from case I, and geometrically nonlinear FEAs are performed for the optimal linear and nonlinear designs in Fig. 6e, f from case II, with the same boundary conditions as in Fig. 6a but excluding the two artificial springs. The parameters used are chosen from those used in the experiment in (Vasista and Tong 2012), and they are $E = 49.5$ MPa and $\nu = 0.292$, thickness of 19 mm and $p = 25$ kPa. Figure 8 depicts the linear and geometrically nonlinear bending-type deformations with the associated von Mises stress contours for the three topologies in Fig. 6b, d, f (the wireframes indicate the un-deformed topological contour). Table 1

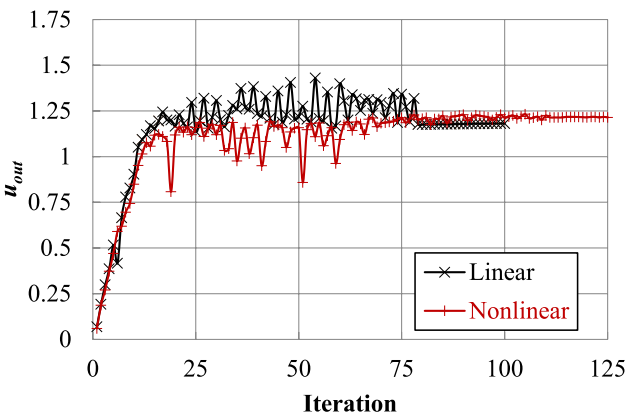

Fig. 7 Objective function convergence history of the unit cell case for both linear and geometrically nonlinear design cases

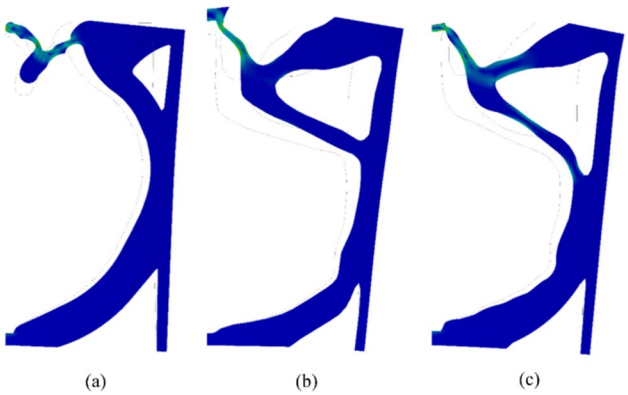

Fig. 8 Schematics of the deformations and the von Mises stress distributions for the optimum topologies in: **a** Fig. 6b using linear FEA; **b** Fig. 6d using linear FEA; and **c** Fig. 6f with geometrical NFEA

Table 1 Linear FEA results of the optimum topologies for case I

Topology and model	Objective function (mm)	Max von Mises stress (MPa)
Figure 6b— u/*p*	4.56	8.75
Figure 6c—equivalent load	8.11	7.97
Figure 6d—linear MSD	9.73	12.41

Table 2 Nonlinear FEA results of the optimum topologies for case II

Topology and model	Objective function (mm)	Max von Mises stress (MPa)
Figure 6e—linear MSD	7.09	11.92
Figure 6f—nonlinear MSD	8.59	8.94

lists the objective functions and the maximum von Mises stresses of the three topologies in case I obtained via the full linear FEAs, and Table 2 presents those for the optimized topologies in case II obtained via the nonlinear FEAs. A comparison among the MSD, equivalent loading and *u/p* results reveals that the objective functions for the topology in Fig. 6d obtained using the present MSD is 213.4 and 120.0% of those for the topologies in Fig. 6b (*u/p*) and Fig. 6c (equivalent loading). A further comparison between the linear and nonlinear MSD topology results indicates that: (a) the objective function increases by 21.2% (nonlinear 8.59 mm vs linear 7.09 mm); and (b) by contrast, the maximum von Mises stress decreases by 25% (nonlinear 8.94 MPa vs linear 11.92 MPa). It is observed that the topologies optimized via the present MSD method maintain a relatively low stress level compared to their large deformations; one contributing factor is believed to be the addition of the strain energy density to the response function ($\alpha > 0$) in Eq. (14). Meanwhile, the addition of the strain energy density term in the response function in Eq. (14) can decrease the output displacement of the compliant mechanisms defined as the objective function in Eqs. (1) or (12). By reducing the weighting of the strain energy density component (or the value of parameter α) in Eq. (14), the output displacement can be further increased with an increased likelihood of overall structural discontinuity simultaneously. However, the output displacement obtained by the present method is significantly higher than that obtained by the *u/P* method, for example, for the case of using $\alpha = 0.3$ in the MSD method compared to the case of $\alpha = 0$ in the *u/P* method.

These results show that the present linear MSD model is capable of creating topologies with larger objective functions than the *u/p* and equivalent loading formulation while maintaining similar maximum von Mises stress, and the nonlinear MSD can further enhance the objective function.

4.3 On the validity and accuracy of MSD

Additional computations are conducted for case II (linear and nonlinear) in benchmark example 4.2 with an alternative topology representation, in which conforming mesh is employed instead of substructures via super-elements for the solid–fluid interface elements. For comparison purposes, the solid–fluid interface elements are subdivided using the strategy shown in Fig. 2b, but conforming meshes are constructed for interface elements instead of substructures via super-elements.

Numerical results show that the NFEA with conforming mesh may diverge and/or terminate prematurely in the iterative optimization processes, where the large deformations of the small triangular fluid elements in the conforming mesh are believed to be the main contributing factor to this observation. Hence, the optimized topologies are taken from case II in Example 4.2 instead, and are re-meshed via the alternative topology representation and solved with the identical linear or nonlinear FEA solution settings. For the linear case (Fig. 6e), the objective function (obj $= u_{\text{out1}} - u_{\text{out2}}$) calculated using the conforming mesh is 1.15, which is only 2.38% less than the present MSD scheme (obj = 1.18). For the nonlinear case (Fig. 6f), the objective function predicted using the conforming mesh is 1.28, which is 4.92% larger than the present MSD scheme (obj = 1.22). The results in this example serve as an evidence to verify the accuracy and effectiveness of the present MSD method.

5 Pressure-actuated PCS

This example presents a practical application of the present topology optimization method, including both numerical and experimental investigations. In this example, the thickness variation of a planar PCS is to be controlled and driven by fluid pressure loads. We formulate the design problems using the proposed MIST method, numerically study the example, and prototype and experimentally test the optimal structures.

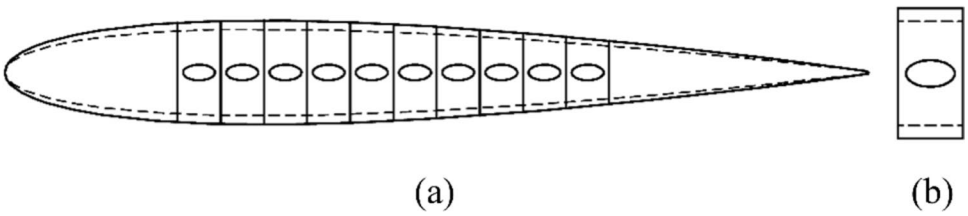

Fig. 9 Schematics of the initial and morphed shapes of **a** an airfoil and **b** a unit cell, where the solid and dashed lines indicate the original and deformed shape

5.1 Design of the pressure-actuated PCS

Let us consider the thickness modulation of a planar structure such as a wing rib achieved via pressure actuating. Figure 9a depicts the concept of a chord-wisely interconnected pressurized cellular structure (PCS) consisting of multiple unit cells as in Fig. 9b for changing the thickness of an individual rib from airfoil NACA 0012 (solid lines) to NACA 0010 (dashed lines). In this section, the PCS design is accomplished through designing separately individual pressurized unit cell and the inter-cellular links.

5.1.1 Design of the unit cell

The design of an individual unit cell can be formulated for a pressurized compliant mechanism problem as in Eq. (12). Figure 10 depicts the design domain, the simplified computational model, and the nonlinear material properties (Polyurethane (ET90ACMOCA) as in (Vasista and Tong 2012; Luo and Tong 2013)). As demonstrated in Fig. 10a, b, the unit cell is internally pressurized at the center, and the output port is located at the midpoint of the top/bottom edge. Thus, the thickness (or height) of the cell can be varied and controlled by internal pressure actuation. In the unit cell design, the objective function is chosen as $-u_{\text{out}}$, and the problem parameters are: the stiffness of the artificial spring attached to the output port $k_{\text{out}} = 10$ N/mm; the virtual force for the nonlinear case $F_{\text{out}} = 50$ N; the volume fraction $V_f = 0.3$ and the applied pressure $p = 0.5$ MPa. The remaining solution parameters are the same as those in the example detailed in Sect. 4.2, except for the filter radius $r_{\min}$ being chosen as 4 times of element size.

The unit cell design problem was solved for three cases: (a) linear case with linear material properties and small displacements, (b) geometrical nonlinear case with linear material properties and large displacements, and (c) geometrical

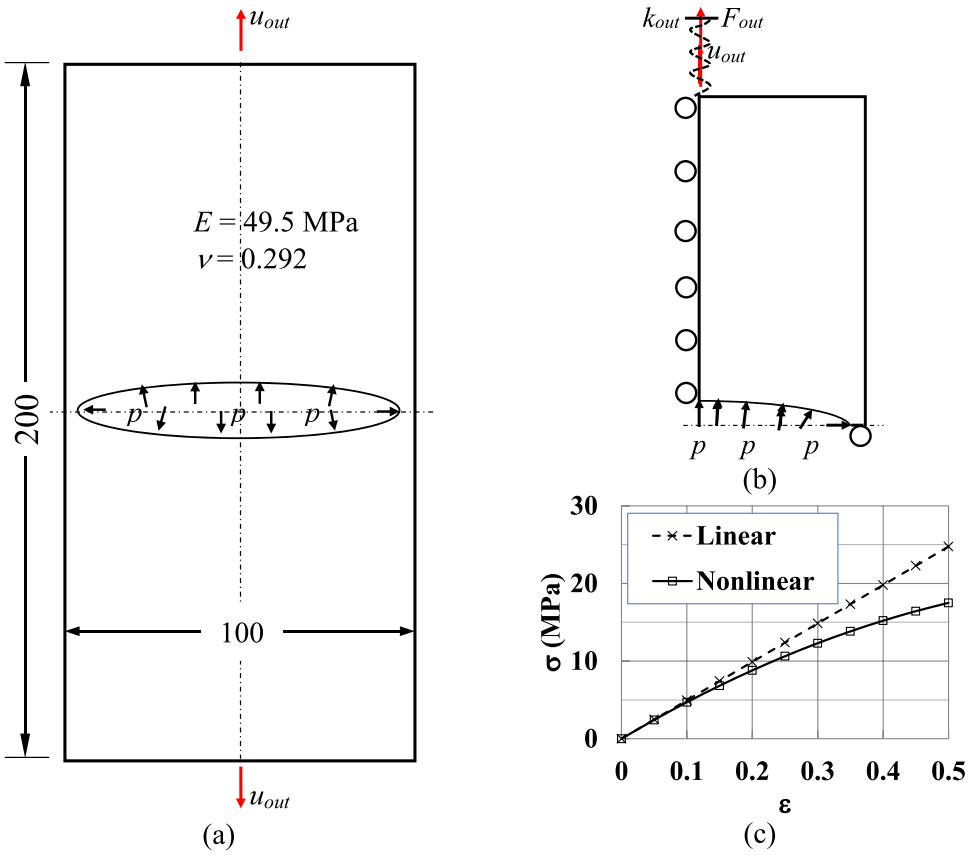

Fig. 10 Unit cell problem: **a** design domain, **b** computational model (with a 25×50 mesh), and **c** material properties for the design of the pressurized unit cell

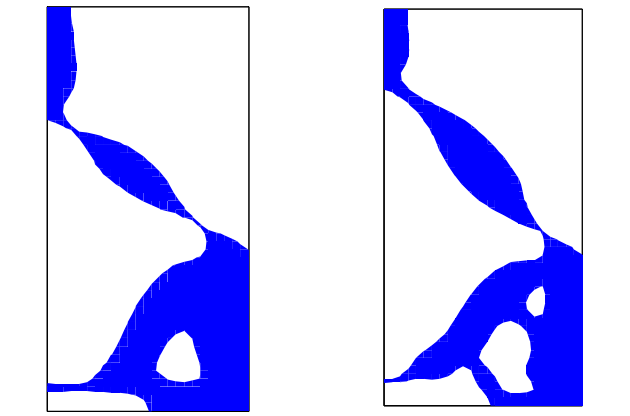

Fig. 11 Optimized topologies and output displacements of a unit cell: **a** linear analysis; **b** geometrically nonlinear analysis

nonlinear case with nonlinear material properties and large displacements. The optimal topologies of case (a) and (b) are presented in Fig. 11a and b, respectively, while the results for case (c) is illustrated in Fig. 12. Figure 12 depicts the convergence history of the objective function ($-u_{\text{out}}$) and the selected topologies for one quarter of a unit cell at iteration 30, 50 100 and 200, respectively. It is worth noting that the pressure surface area for case (c) is much larger than those for cases (a) and (b), according to Figs. 11 and 12. The unit cell constructed from the converged quarter cell topology in Fig. 12 can then be used to generate pressurized cellular network for potential applications, such as the airfoil rib as in Fig. 9.

5.1.2 Design of the link

The design of cellular links is accomplished via solving a typical single–input–single–output compliant mechanism problem, in which a horizontal displacement at an input port is transferred to a vertical displacement at an output port. To formulate such a problem, a full NFEA of the whole optimum unit cell was conducted to understand its overall deformation and von Mises stress distribution as shown in Fig. 13a (under a pressure of 0.576 MPa). Figure 13b shows the variation of the horizontal displacement (u_x) along the right edge with $x = 50$ and $0 \le y \le 40$ (with reference to the dimensions in Fig. 10a). In light of the horizontal displacement distribution in Fig. 13b, four cellular links attached to the unit cell at $x = \pm 50$ and $y = \pm 15$ are chosen with each having a rectangular design domain 30×15. Figure 13c depicts the quarter computational model of 15×7.5 for the cellular link in the first quadrant simplified with a further assumption of local symmetry. As no pressure load is involved in the link design, the strain energy and the Φ function in previous iteration will not be included in the objective function (i.e. $\alpha = 0$, $k = 1$). Figure 13d depicts the optimized topology of the link computed by the present algorithm considering material and geometrical nonlinearities. In this computation, $V_f = 0.3$; $F_{in} = 20$ N; $F_{\text{out}} = 10$ N; $k_{\text{in}} = 5$ N/mm; $k_{\text{out}} = 10$ N/mm.

5.2 Experimental verification

5.2.1 Sample fabrication

The optimized unit cell designs, as shown in Fig. 12, were fabricated using polyurethane (ET90A + MOCA). The specimens were cut from a polyurethane plate of 19 mm thick by

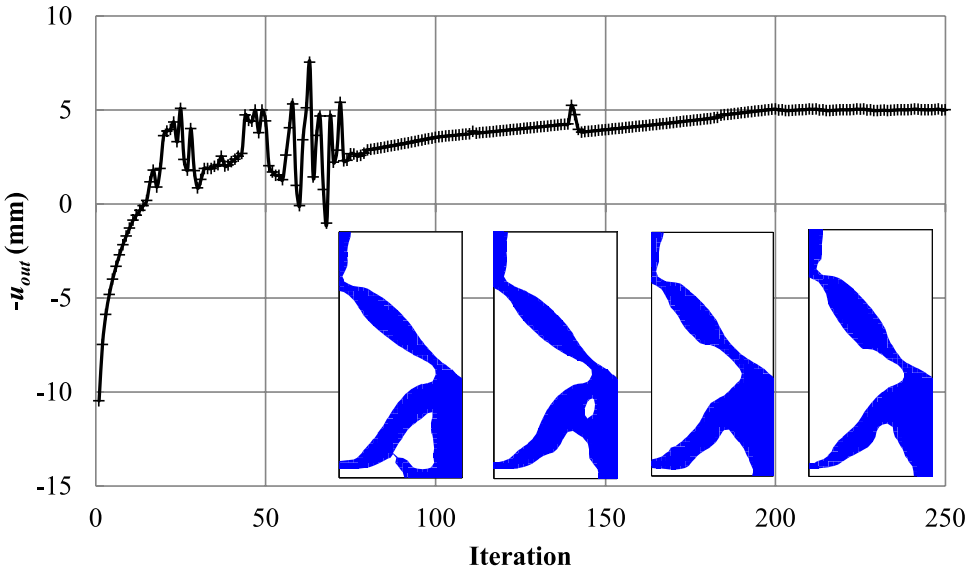

Fig. 12 The convergence history of the objective function for the design considering both material and geometrical nonlinearity and the selected topologies for one quarter of a unit cell at iterations 30, 50, 100 and 200 (from left to right)

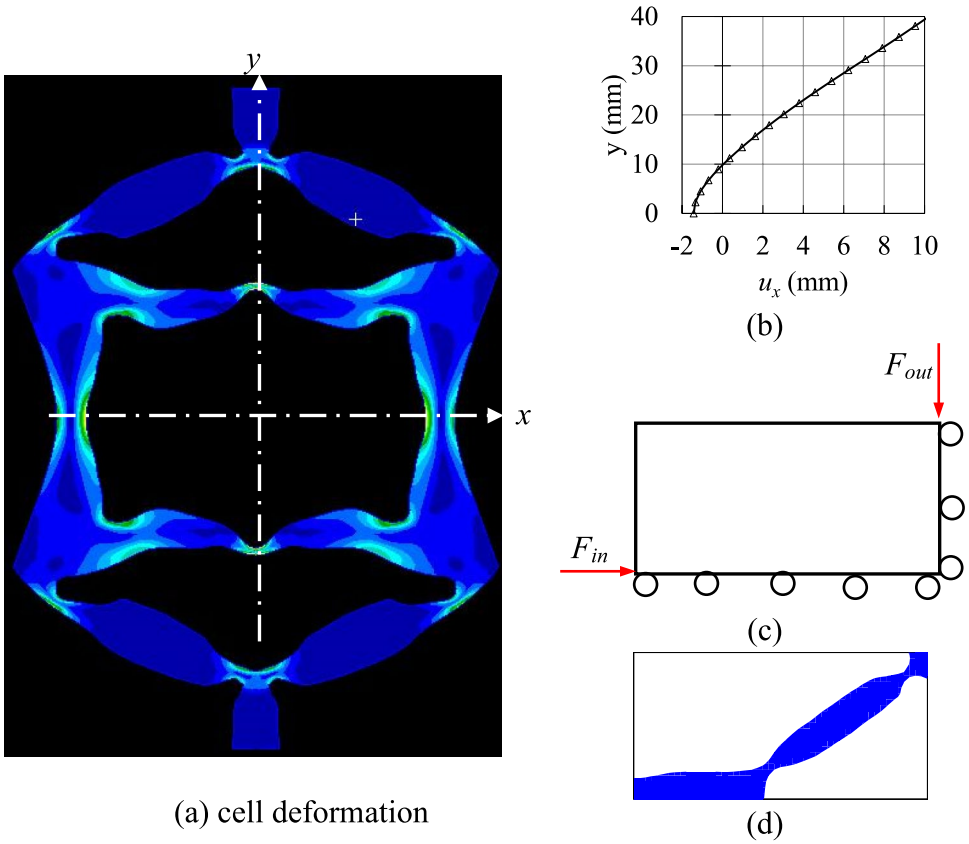

Fig. 13 Deformation of the unit cell at $p = 0.576$ MPa and link design **a** deformation and nonlinear von Mises stress distribution; **b** displacement u_x of the right edge along y axis; **c** model for optimal design of the link (mesh: 50×25); and **d** the optimized topology

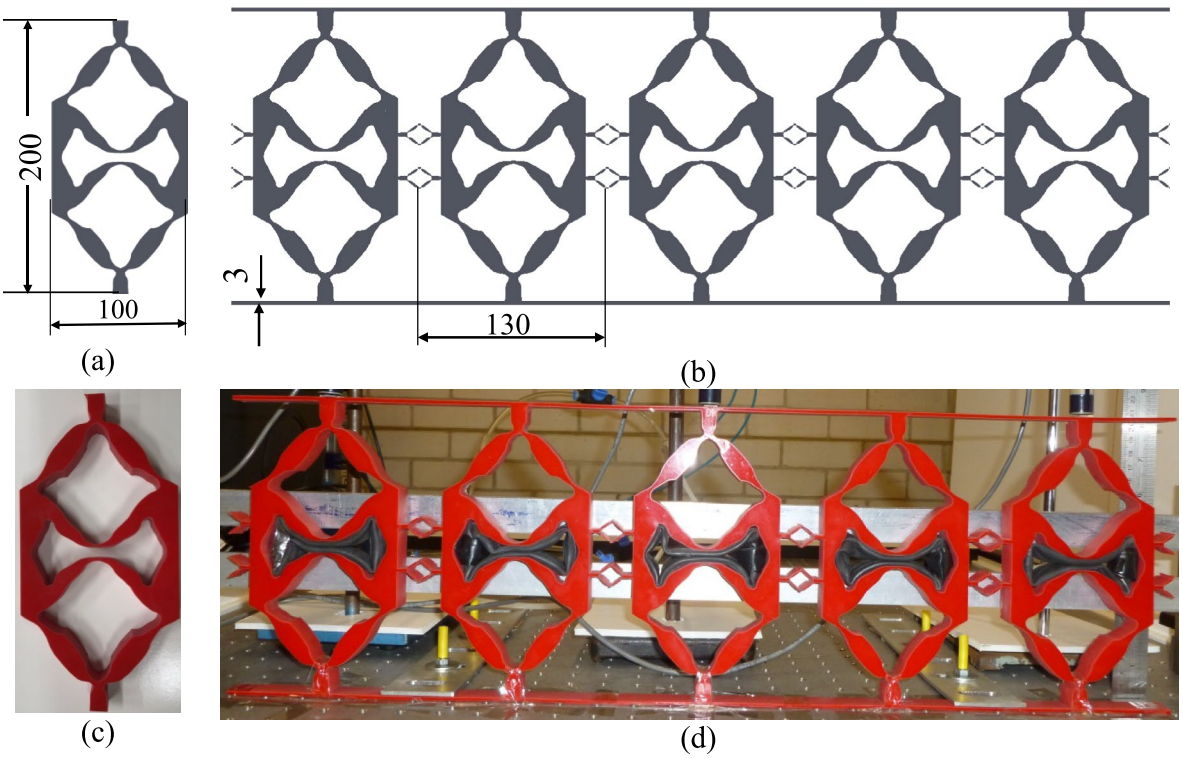

Fig. 14 Designs of pressurized cellular structure (PCS) **a** the optimized design of the unit cell; **b** the PCS design with 5 parallel cells; **c** specimen of the unit cell; **d** the PCS with the embedded bladders

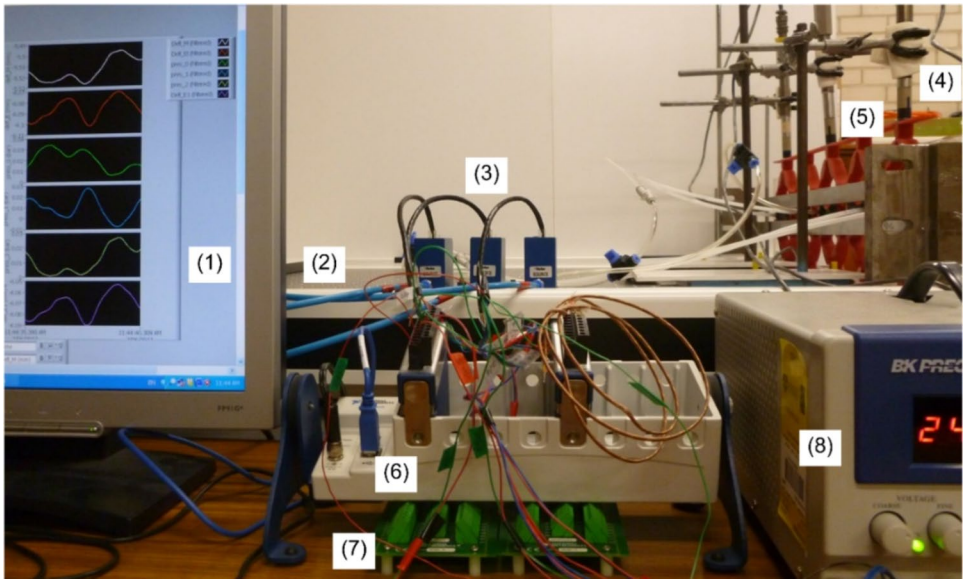

Fig. 15 Experimental set-up: (1) computer system; (2) anti-vibration table; (3) pressure controllers; (4) displacement sensors; (5) specimen; (6) data logger; (7) signal controller (8) DC power supply

using a water-jet technology, as shown in Fig. 14c and d. Air pressures are applied to the unit cells by air bladders, as in Fig. 14d.

5.2.2 Test of the unit cell

Figure 15 depicts the experimental setup with the used equipment and instruments, e.g., the miniature electronic

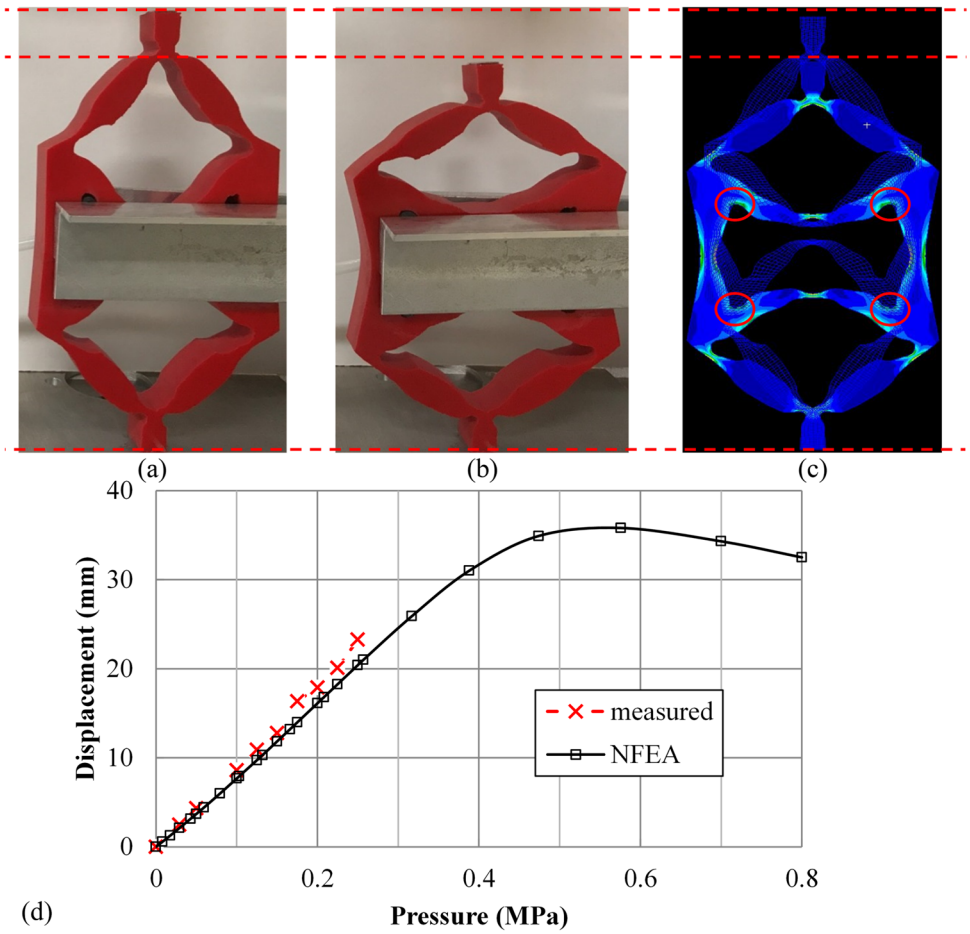

Fig. 16 The deformations of the unit cell specimen results **a** the un-deformed specimen; **b** the deformed specimen under $p = 0.25$ MPa; **c** the deformed cell under $p = 0.25$ MPa predicted by NFEA; **d** a comparison of the measured and NFEA predicted displacement–pressure curves for the unit cell specimen

Table 3 Air pressures (MPa) in cells 1–5 of 3 loading case

Cases	Video	Cell 1	Cell 2	Cell 3	Cell 4	Cell 5
1	1	0.2	0.15	0.2	0.15	0.1
2	2	0.2	0.15	0.1	0.15	0.2
3	3	0.1	0.2	0.15	0.2	0.15

pressure controller controls output pressures of three channels, the data logger records displacements and input air pressures, the signal controller controls air pressure output, and displacement sensors measure displacements. Similar to the experiment in (Vasista and Tong 2012), pneumatic pressure was applied to the inner rubber bladders. LabVIEW software was used to program and conduct all the tests by controlling the pressure channel and measuring the in situ pressures and displacements.

Figure 16a, b depicts the test results of the unit cell specimen and its comparison with the NFEA results when subjected to a pressure of 0.25 MPa. Figure 16b and c indicate a good agreement between the measured and predicted deformations, and both cases show that large deformation can be generated. Figure 16d depicts a comparison between the measured and NFEA predicted displacement–pressure curves. At the pressure of 0.25 MPa, the measured displacement of the top surface of the unit cell specimen is 23.8 mm, and the NFEA predicted one is 20.4 mm. The relative difference between the NFEA and measured displacements is 14.3%. It is believed that one major contributing factor to this difference is related to the pressure application method

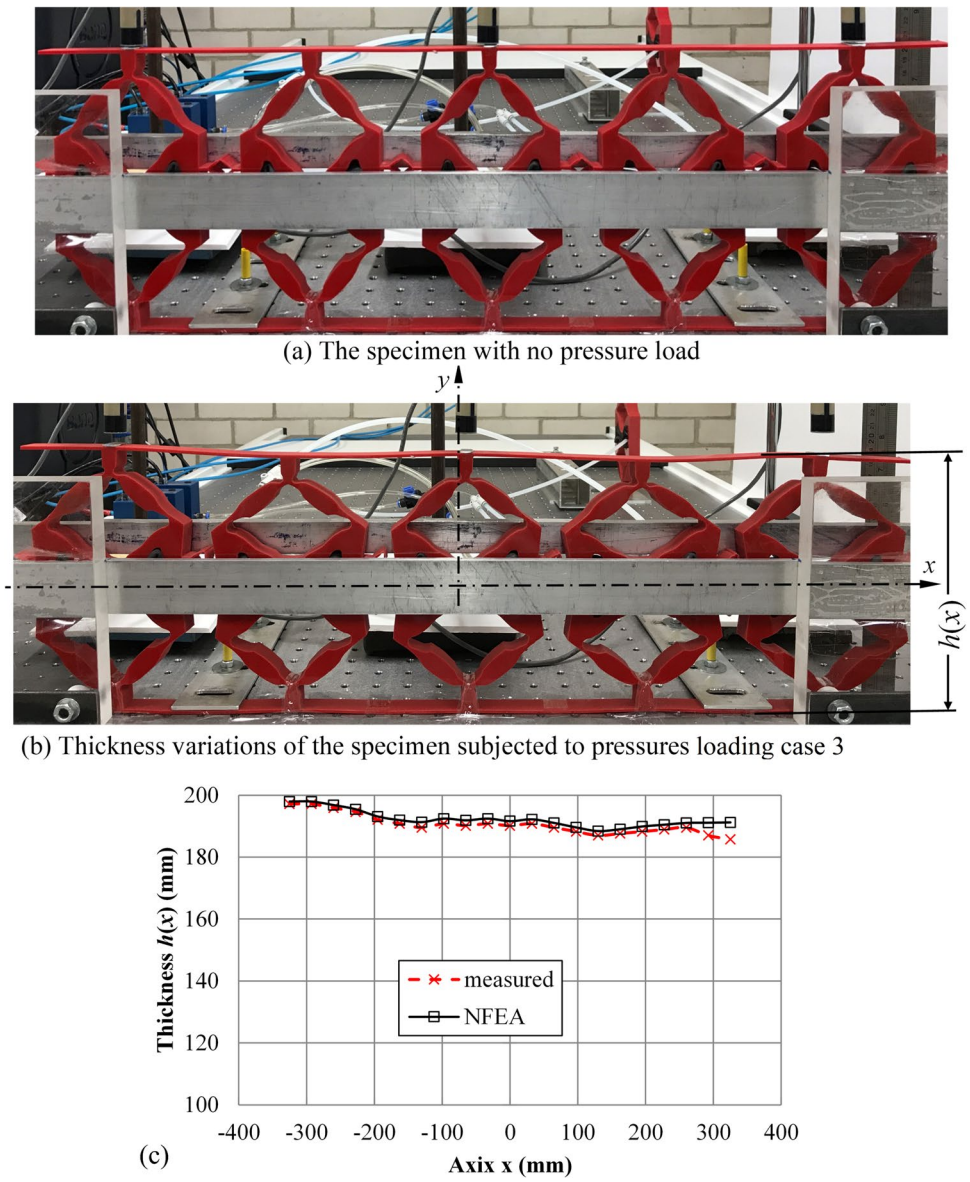

(a) The specimen with no pressure load

(b) Thickness variations of the specimen subjected to pressures loading case 3

(c)

Fig. 17 **a** the PCS specimen without pressure loading; **b** the deformation profile of the PCS specimen and **c** a comparison between the measured and NFEA predicted thickness variations under the pressure load case 3 for the five cells (from left to right)

using inner rubber bladders, which probably applies small or minimum pressure to the four corners, as marked with circles in Fig. 16c. The contraction ratio (displacement/total thickness) of the experimental results is 11.9%.

5.2.3 Test of the PCS

The five-cell PCS specimen was tested to illustrate its thickness changing capability. Videos 1–3 illustrate the movements of the PCS for the 3 loading cases in Table 3. Pressures linearly increase from 0 to the specified values and then linearly decrease to zero.

Figure 17a depicts the PCS specimen with no pressure applied. Figure 17b depicts the deformation of case 3 when cells 1 to 5 (counted from left to right) are respectively subjected to different pressures simultaneously. As the lower sheet of the PCS specimen is fixed, the height contraction is used to demonstrate the thickness change. Figure 17c depicts a comparison between the measured and NFEA predicted height reductions of the PCS specimen along the horizontal direction originated from the center of cell 3. Figure 17c indicates that there exists a good correlation between the measured height variations and the NFEA predictions, in particular at the middle lines of the five cells, i.e. $x=0,\pm 130,\pm 260$. A small discrepancy in the free cantilever section of the upper sheet at the right end of cell 5 exists, and this could be due to an improper deformation of cell 5 caused by the non-uniform pressure. As shown in Fig. 17b, c, a non-uniform height variation of up to 6.4% of the maximum thickness (200 mm) can be achieved for the pressure load case. This example illustrates that the current PCS design is capable of changing the airfoil as shown in Fig. 9 through application of different pressures to all unit cells.

6 Conclusion

This study presents a novel mixed substructure-density model for topology representation and update in optimum design of pressurized compliant structures taking into account of geometrical and material nonlinearity. The present model is capable of capturing key geometrical and structural features, such as solid–fluid interfaces and equivalent stiffness matrices and load vectors. An algorithm is developed by implementing this model via super-elements and a combined update scheme based on a moving isosurface threshold method, in which the response function is constructed using both current and previous iterations. Numerical examples and experiments are presented to verify the present model and algorithm. Those results show that the proposed model and algorithm can generate topological designs of compliant mechanisms with larger objective functions (output displacements) and deformations compared to those in the literature for linear analysis, and can further improve output displacements when nonlinearities are taken into consideration. The experimental results for the unit cell and the PCS specimens illustrate the feasibility of achieving possible airfoil thickness changes via applying differential cell pressures.

Appendix: Derivation of nonlinear strain energies

By assuming that loads (1) and (2) be virtual and real, respectively, and using the principle of virtual work at the τth load step, one can obtain:

$$\int_0^{{}^{\tau}\boldsymbol{u}^{(2)}} \boldsymbol{F}^{(l)T} d\boldsymbol{u}^{(2)} = \int_{\Omega} \left(\int_0^{{}^{\tau}\boldsymbol{\varepsilon}^{(2)}} \boldsymbol{S}^{(l)T} d\boldsymbol{\varepsilon}^{(2)} \right) d\Omega (l = 1,2; = 1,2, \ldots, M) \tag{A1}$$

Subtracting the external virtual work and internal virtual energy at the τth load step from those at the $\tau-1$th load step yields:

$$\int_{{}^{\tau-1}\boldsymbol{u}^{(2)}}^{{}^{\tau}\boldsymbol{u}^{(2)}} \boldsymbol{F}^{(l)T} d\boldsymbol{u}^{(2)} = \int_{\Omega} \left(\int_{{}^{\tau-1}\boldsymbol{\varepsilon}^{(2)}}^{{}^{\tau}\boldsymbol{\varepsilon}^{(2)}} \boldsymbol{S}^{(l)T} d\boldsymbol{\varepsilon}^{(2)} \right) d\Omega (l = 1,2; = 1,2, \ldots, M) \tag{A2}$$

By using the trapezium formula to evaluate the integrals, Eq. (A2) can be approximated as:

$$\left({}^{\tau}\boldsymbol{F}^{(l)} + {}^{\tau-1}\boldsymbol{F}^{(l)}\right)^T \left({}^{\tau}\boldsymbol{u}^{(2)} - {}^{\tau-1}\boldsymbol{u}^{(2)}\right) = \int_{\Omega} \left({}^{\tau}\boldsymbol{S}^{(l)T} + {}^{\tau-1}\boldsymbol{S}^{(l)T}\right)\left({}^{\tau}\boldsymbol{\varepsilon}^{(2)} - {}^{\tau-1}\boldsymbol{\varepsilon}^{(2)}\right) d\Omega \tag{A3}$$

Noting ${}^{\tau}\boldsymbol{F}^{(l)} = {}^{\tau}\Delta\boldsymbol{F}^{(l)}$, Eq. (A3) can be rewritten as

$$\boldsymbol{F}^{(l)T}\left({}^{\tau}\boldsymbol{u}^{(2)} - {}^{\tau-1}\boldsymbol{u}^{(2)}\right) = \int_{\Omega} \left(\frac{{}^{\tau}\boldsymbol{S}^{(l)T} + {}^{\tau-1}\boldsymbol{S}^{(l)T}}{{}^{\tau}\Delta + {}^{\tau-1}\Delta} \right)\left({}^{\tau}\boldsymbol{\varepsilon}^{(2)} - {}^{\tau-1}\boldsymbol{\varepsilon}^{(2)}\right) d\Omega \tag{A4}$$

where the load step$\tau = 1, 2, \ldots, M$.

Summing all the M equations in Eq. (A4) for all τ from 1 to M yields:

$$\boldsymbol{F}^{(l)T}\left({}^{M}\boldsymbol{u}^{(2)} - {}^{0}\boldsymbol{u}^{(2)}\right) = \int_{\Omega} \left[\sum_{\tau=1}^{M} \left(\frac{{}^{\tau}\boldsymbol{S}^{(l)T} + {}^{\tau-1}\boldsymbol{S}^{(l)T}}{{}^{\tau}\Delta + {}^{\tau-1}\Delta} \right)\left({}^{\tau}\boldsymbol{\varepsilon}^{(2)} - {}^{\tau-1}\boldsymbol{\varepsilon}^{(2)}\right) \right] d\Omega \tag{A5}$$

where the load case $l = 1, 2$.

Let us assume: ${}^{0}\mathbf{u}^{(2)} = {}^{0}\boldsymbol{\varepsilon}^{(2)} = {}^{0}\mathbf{S}^{(2)} = 0$, Eq. (A5) becomes:

$$\boldsymbol{F}^{(l)T M}\boldsymbol{u}^{(2)} = \int_{\Omega} \left[\sum_{\tau=1}^{M} \left(\frac{{}^{\tau}\boldsymbol{S}^{(l)T} + {}^{\tau-1}\boldsymbol{S}^{(l)T}}{{}^{\tau}\Delta + {}^{\tau-1}\Delta} \right)\left({}^{\tau}\boldsymbol{\varepsilon}^{(2)} - {}^{\tau-1}\boldsymbol{\varepsilon}^{(2)}\right) \right] d\Omega (l = 1,2) \tag{A6}$$

As demonstrated in Eq. (A6), the nonlinear strain and mutual strain energy can be expressed using trapezium

area sums for all load steps. In this work, it is further approximated using only one segment from load step $\tau = 0$ to M as:

$$\boldsymbol{F}^{(l)TM}\boldsymbol{u}^{(2)} = \int_{\Omega} \left[\frac{{}^{M}\boldsymbol{S}^{(l)TM}\boldsymbol{\varepsilon}^{(2)}}{{}^{M}\Delta} \right] d\Omega (l = 1, 2) \tag{A7}$$

Supplementary Information The online version contains supplementary material available at https://doi.org/10.1007/s00158-024-03944-2.

Acknowledgments The authors are grateful for the support of the Australian Research Council via Discovery-Project Grants DP170104916.

Funding Open Access funding enabled and organized by CAUL and its Member Institutions.

Declarations

Conflict of interest On behalf of all authors, the corresponding author states that there is no conflict of interest.

Replication of Results The necessary information for replicating the results is presented in the manuscript. Further details regarding the implementation are available upon request from the corresponding author.

References

Bandi P, Tovar A, Renaud JE (2011) Design of 2d and 3d non-linear compliant mechanisms using hybrid cellular automata. In: Proceedings of the 52nd AIAA structures, structural dynamics, and materials conference.

Banh TT, Shin S, Kang J, Lee D (2024) Frequency-constrained topology optimization in incompressible multi-material systems under design-dependent loads. Thin-Walled Struct 196:111467

Bathe K-J (1996) Finite element procedures. Prentice Hall, Englewood Cliffs

Bendsoe MP, Sigmund O (2003) Topology optimization: theory, methods and applications. Springer, Berlin, New York

Bruns TE, Tortorelli DA (2001) Topology optimization of non-linear elastic structures and compliant mechanisms. Comput Meth Appl Mech Eng 190(26–27):3443–3459. https://doi.org/10.1016/s0045-7825(00)00278-4

Buhl T, Pedersen CBW, Sigmund O (2000) Stiffness design of geometrically nonlinear structures using topology optimization. Struct Multidisc Optim 19(2):93–104. https://doi.org/10.1007/s001580050089

Chen B-C, Kikuchi N (2001) Topology optimization with design-dependent loads. Finite Elem Anal des 37(1):57–70. https://doi.org/10.1016/S0168-874X(00)00021-4

Chen B-C, Silva ECN, Kikuchi N (2001) Advances in computational design and optimization with application to MEMS. Int J Numer Meth Eng 52(1–2):23–62. https://doi.org/10.1002/nme.271

de Souza EM, Silva ECN (2020) Topology optimization applied to the design of actuators driven by pressure loads. Struct Multidisc Optim 61(5):1763–1786. https://doi.org/10.1007/s00158-019-02421-5

Du J, Olhoff N (2004) Topological optimization of continuum structures with design-dependent surface loading - Part I: new computational approach for 2D problems. Struct Multidisc Optim 27(3):151–165. https://doi.org/10.1007/s00158-004-0379-y

Frecker MI, Ananthasuresh GK, Nishiwaki S, Kikuchi N, Kota S (1997) Topological synthesis of compliant mechanisms using multi-criteria optimization. J Mech Des Trans ASME 119(2):238–245. https://doi.org/10.1115/1.2826242

Fu J, Xia L, Gao L, Xiao M, Li H (2019) Topology optimization of periodic structures with substructuring. J Mech Des 141 (7). https://doi.org/10.1115/1.4042616

Hammer VB, Olhoff N (2000) Topology optimization of continuum structures subjected to pressure loading. Struct Multidisc Optim 19(2):85–92. https://doi.org/10.1007/s001580050088

Huang M, Cui T, Liu C, Du Z, Zhang J, He C, Guo X (2023) A Problem-Independent Machine Learning (PIML) enhanced substructure-based approach for large-scale structural analysis and topology optimization of linear elastic structures. Extreme Mech Lett 63:102041. https://doi.org/10.1016/j.eml.2023.102041

Ibhadode O, Zhang Z, Rahnama P, Bonakdar A, Toyserkani E (2020) Topology optimization of structures under design-dependent pressure loads by a boundary identification-load evolution (BILE) model. Struct Multidisc Optim 62:1865–1883

Jenkins N, Maute K (2016) An immersed boundary approach for shape and topology optimization of stationary fluid-structure interaction problems. Struct Multidisc Optim 54(5):1191–1208. https://doi.org/10.1007/s00158-016-1467-5

Jiang Y, Zhao M (2020) Topology optimization under design-dependent loads with the parameterized level-set method based on radial-basis functions. Comput Methods Appl Mech Eng 369:113235

Jung D, Gea HC (2004) Compliant mechanism design with non-linear materials using topology optimization. Int J Mech Mater des 1(2):157–171. https://doi.org/10.1007/s10999-004-1494-z

Knippers J, Speck T (2012) Design and construction principles in nature and architecture. Bioinspir Biomim 7(1):015002

Kumar P (2023) TOPress: a MATLAB implementation for topology optimization of structures subjected to design-dependent pressure loads. Struct Multidisc Optim 66(4):97

Kumar P, Langelaar M (2021) On topology optimization of design-dependent pressure-loaded three-dimensional structures and compliant mechanisms. Int J Numer Meth Eng 122(9):2205–2220

Kumar P, Langelaar M (2022) Topological synthesis of fluidic pressure-actuated robust compliant mechanisms. Mech Mach Theory 174:104871. https://doi.org/10.1016/j.mechmachtheory.2022.104871

Kumar P, Frouws JS, Langelaar M (2020) Topology optimization of fluidic pressure-loaded structures and compliant mechanisms using the Darcy method. Struct Multidisc Optim 61(4):1637–1655. https://doi.org/10.1007/s00158-019-02442-0

Lienhard J, Schleicher S, Poppinga S, Masselter T, Milwich M, Speck T, Knippers J (2011) Flectofin: a hingeless flapping mechanism inspired by nature. Bioinspir Biomim 6(4):045001

Liu Z, Xia L, Xia Q, Shi T (2020) Data-driven design approach to hierarchical hybrid structures with multiple lattice configurations. Struct Multidisc Optim 61(6):2227–2235. https://doi.org/10.1007/s00158-020-02497-4

Liu Y, Gao R, Li Y, Fang D (2024) EMsFEM based concurrent topology optimization method for hierarchical structure with multiple substructures. Comput Methods Appl Mech Eng 418:116549. https://doi.org/10.1016/j.cma.2023.116549

Lu Y, Tong L (2021) Topology optimization of compliant mechanisms and structures subjected to design-dependent pressure loadings. Struct Multidisc Optim 63(4):1889–1906. https://doi.org/10.1007/s00158-020-02786-y

Lu Y, Tong L (2024) Topology and orientation optimization of multi-material hinge-free composite compliant mechanisms under multiple design-dependent loadings. Struct Multidisc Optim 67(2):17. https://doi.org/10.1007/s00158-023-03723-5

Luo Q, Tong L (2013) Adaptive pressure-controlled cellular structures for shape morphing: II. Numerical and experimental validation. Smart Mater Struct 22(5):055015

Luo Q, Tong L (2016) An algorithm for eradicating the effects of void elements on structural topology optimization for nonlinear compliance. Struct Multidisc Optim 53(4):695–714. https://doi.org/10.1007/s00158-015-1325-x

Ma Z-D, Kikuchi N, Pierre C, Raju B (2005) Multidomain topology optimization for structural and material designs. J Appl Mech 73(4):565–573. https://doi.org/10.1115/1.2164511

Panganiban H, Jang GW, Chung TJ (2010) Topology optimization of pressure-actuated compliant mechanisms. Finite Elem Anal des 46(3):238–246. https://doi.org/10.1016/j.finel.2009.09.005

Picelli R, Vicente WM, Pavanello R (2015) Bi-directional evolutionary structural optimization for design-dependent fluid pressure loading problems. Eng Optim 47(10):1324–1342. https://doi.org/10.1080/0305215x.2014.963069

Picelli R, Neofytou A, Kim HA (2019) Topology optimization for design-dependent hydrostatic pressure loading via the level-set method. Struct Multidisc Optim 60(4):1313–1326. https://doi.org/10.1007/s00158-019-02339-y

Schleicher S, Lienhard J, Poppinga S, Speck T, Knippers J (2015) A methodology for transferring principles of plant movements to elastic systems in architecture. Comput Aided des 60:105–117

Sigmund O, Clausen PM (2007) Topology optimization using a mixed formulation: an alternative way to solve pressure load problems. Comput Methods Appl Mech Eng 196(13–16):1874–1889. https://doi.org/10.1016/j.cma.2006.09.021

Tong LY, Lin JZ (2011) Structural topology optimization with implicit design variable-optimality and algorithm. Finite Elem Anal des 47(8):922–932. https://doi.org/10.1016/j.finel.2011.03.004

Vasista S, Tong LY (2012) Design and testing of pressurized cellular planar morphing structures. AIAA J 50(6):1328–1338. https://doi.org/10.2514/1.j051427

Vasista S, Tong L (2013) Topology-optimized design and testing of a pressure-driven morphing-aerofoil trailing-edge structure. AIAA J 51(8):1898–1907. https://doi.org/10.2514/1.j052239

Vasista S, Tong L (2014) Topology optimisation via the moving iso-surface threshold method: implementation and application. Aeronaut J 118(1201):315–342

Wu Z, Xia L, Wang S, Shi T (2019) Topology optimization of hierarchical lattice structures with substructuring. Comput Methods Appl Mech Eng 345:602–617. https://doi.org/10.1016/j.cma.2018.11.003

Xia Q, Wang MY, Shi T (2015) Topology optimization with pressure load through a level set method. Comput Methods Appl Mech Eng 283:177–195. https://doi.org/10.1016/j.cma.2014.09.022

Yoon GH, Kim YY (2007) Topology optimization of material-nonlinear continuum structures by the element connectivity parameterization. Int J Numer Meth Eng 69(10):2196–2218

Zhang H, Zhang X, Liu S (2008) A new boundary search scheme for topology optimization of continuum structures with design-dependent loads. Struct Multidisc Optim 37(2):121–129. https://doi.org/10.1007/s00158-007-0221-4